Tissue and Cell 73 (2021) 101659

Contents lists available at ScienceDirect

Tissue and Cell

journal homepage: www.elsevier.com/locate/tice

Detection of malignant melanoma in H&E-stained images using deep learning techniques

Salah Alheejawi [a], Richard Berendt [b], Naresh Jha [b], Santi P. Maity [c], Mrinal Mandal [a,*]

[a] Department of Electrical and Computer Engineering, University of Alberta, Edmonton, AB, Canada
[b] Department of Medicine, University of Alberta, Edmonton, AB, Canada
[c] Department of Information Technology, Indian Institute of Engineering Science and Technology, Shibpur, India

ARTICLE INFO

Keywords:
Histopathological image analysis
Nuclear segmentation
Melanoma detection
Deep learning

ABSTRACT

Histopathological images are widely used to diagnose diseases including skin cancer. As digital histopathological images are typically of very large size, in the order of several billion pixels, automated identification of all abnormal cell nuclei and their distribution within multiple tissue sections would assist rapid comprehensive diagnostic assessment. In this paper, we propose a deep learning-based technique to segment the melanoma regions in Hematoxylin and Eosin (H&E) stained histopathological images. In this technique, the nuclei in the image are first segmented using a Convolutional Neural Network (CNN). The segmented nuclei are then used to generate melanoma region masks. Experimental results with a small melanoma dataset show that the proposed method can potentially segment the nuclei with more than 94 % accuracy and segment the melanoma regions with a Dice coefficient of around 85 %. The proposed technique also has a small execution time making it suitable for clinical diagnosis with a fast turnaround time.

1. Introduction

Cutaneous Malignant Melanoma (CMM) is an aggressive type of skin cancer. The early diagnosis of melanoma is very important as it helps to increase the chances of successful treatment and may increase survival rate (Brochez et al., 2002). The gold standard of the diagnosis is through the examination of histopathological images. The digitized histopathological slides, which are typically obtained by staining and scanning the biopsy slides of the skin tissue, can provide the cell morphological features with a high resolution. The digitized slides are known as Whole Slide Images (WSIs) and computer aided diagnosis (CAD) techniques can speed up detection of cancer features resulting in a fast diagnosis by the pathologist (Alheejawi et al., 2019). Pathologists generally use Haematoxylin and Eosin (H&E) stained images as the morphological features of the melanocytes and other cells become vividly clear. In H&E-stained image, the cell nuclei (as they contain chromatin) are typically observed in the blue shade while the cytoplasm and other connective tissues are observed with the varying shades of pink (Lu et al., 2013a).

Fig. 1 shows an H&E-stained histopathological image of a CMM within a cross section of the skin tissue. The epidermis layer in the Fig.1 is contoured with the green color, and the CMM is contoured in brown color. Note that in this image the CMM are contoured manually by morphology. The skin tissues diagnosed with melanoma typically contain regions of inflammatory cells (as shown in blue contour) near the CMM regions. In the enlarged patch, it is observed that the abnormal melanocytes appear with irregularity in shape and color intensity (Rojo et al., 2011; Weinstein et al., 2009) whereas the inflammatory cells mainly appear in dark color with dense nuclei. Table 1 shows cells features in detail that can be shown in skin tissue diagnosed with melanoma.

There have been recent reports of melanoma diagnosis based on the histopathological image analysis (Cheng et al., 2012; Lu et al., 2013b; Cheng and Mandal, 2015; Hongming et al., 2013). Investigators have focused on the detection of the nuclei (Cheng et al., 2012), detection of the melanocytes (Lu et al., 2013b), and the melanoma classification of WSIs (Cheng and Mandal, 2015). Xu et al. (Hongming et al., 2013) proposed an automated technique (henceforth referred to as the Watershed + Voting technique) to segment the cell nuclei in H&E-stained images. The technique detects the nuclei seeds by using voting areas and segments the nuclei cells using marked watershed algorithm. The technique has been shown to provide a good performance,

* Corresponding author.
E-mail addresses: alheejaw@ualberta.ca (S. Alheejawi), richard.berendt@albertahealthservices.ca (R. Berendt), naresh.jha@albertahealthservices.ca (N. Jha), santipmaity@it.iiests.ac.in (S.P. Maity), mmandal@ualberta.ca (M. Mandal).

https://doi.org/10.1016/j.tice.2021.101659
Received 6 April 2021; Received in revised form 25 September 2021; Accepted 27 September 2021
Available online 29 September 2021

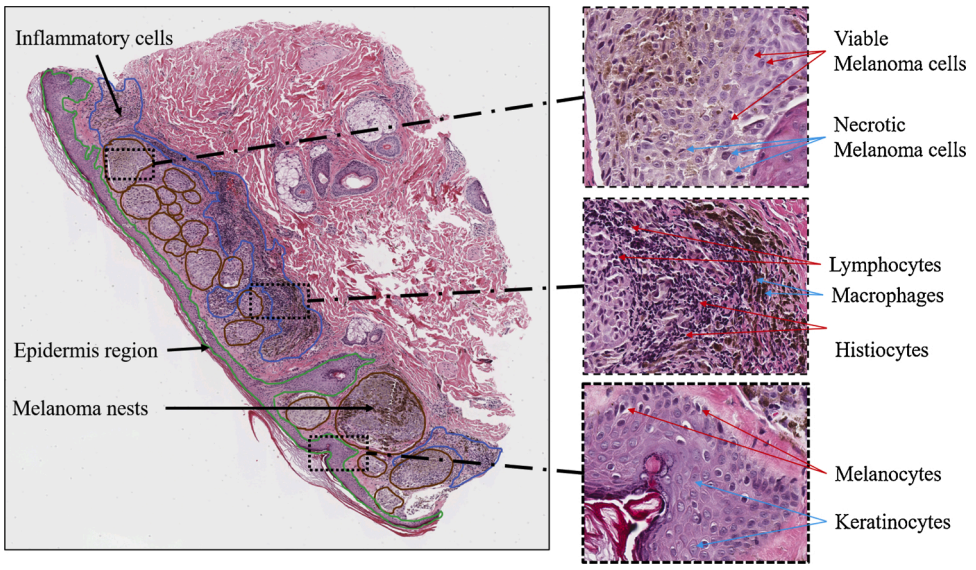

Fig. 1. Histopathological image of a skin tissue with cutaneous malignant melanoma. The epidermis region, the melanoma nests and inflammatory cells are contoured in green, brown and blue colors, respectively.

Table 1
Cells types and comparisons within skin tissue sections diagnosed with melanoma.

Cells		Features
Melanoma tumour cells	Viable Melanoma cells	Very large size (>15–50 μm in diameter) with abundant cytoplasm sometimes containing brown melanin pigment, pleomorphic large vesicular nuclei, and prominent often multiple nucleoli, with frequent mitoses.
	Necrotic Melanoma cells	Size may decrease, nuclei may become smaller and darker compared with viable Melanoma cells.
Inflammatory cells	Lymphocytes	Much smaller size (7–12 μm in diameter), with dark nucleus, little cytoplasm and elliptical boundaries.
	Histiocytes/ Macrophages	Moderate to large size (20–40 μm in diameter), with dark nucleus, and irregular boundaries. Macrophage cytoplasm may contain consumed brown melanin pigment.
Epidermis cells	Melanocytes	Small to moderate size (7–20 μm in diameter), large dark nucleus, situated at the Dermal-Epidermal junction.
	Keratinocytes, Langerhans and Merkel	Variable size with differentiation (15–50 μm in diameter), dark nucleus, and variably abundant eosinophilic cytoplasm.

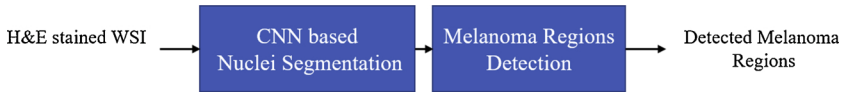

Fig. 2. Schematic of the proposed melanoma detection technique.

but it has a high computational complexity due to presence of the seed detection algorithm. Xu et al. (2017a) proposed another cell nuclei segmentation technique (henceforth referred to as the gLoG + mRLS technique). This technique first detects the nuclei seeds using the generalized Laplacian of Gaussian (gLoG) filters and then segments the cells using multiple Radial Lines Scanning (mRLS) algorithm. The mRLS uses high gradient pixel locations and shape information to accurately segment the cell nuclei (Xu et al., 2017b).

The nuclei detection techniques (Hongming et al., 2013; Xu et al., 2017b) mentioned above are generally based on the extracted hand-crafted features that require significant time for calculation. Furthermore, these manually designed features are often over-specified or incomplete. On the other hand, features learned using the deep learning algorithms are easy to adapt and fast to learn, hence, Convolutional Neural Network (CNN) have recently been used successfully in medical image analysis. Badrinarayanan et al. (2015) proposed the SegNet architecture for the object segmentation. Ronneberger et al. (2015) proposed the U-Net architecture for biomedical image segmentation. Alheejawi et al. (2020) proposed a technique (henceforth referred to as the NS-Net + FC technique) to segment and classify the cell nuclei on the H&E-stained images. The segmentation is performed using the NS-Net architecture that contains 5 convolutional layers with different filter sizes. From each segmented nucleus, 54 features are extracted, and these feature vectors are fed to a Support Vector Machine (SVM) for nuclei classification (melanoma or non-melanoma nuclei). Patrik et al. (Sabol et al., 2021) proposed a technique to perform patch-based segmentation of the H&E-stained WSI for diagnosing colorectal cancer. The proposed patch-based segmentation technique (henceforth referred to as the PBS-ResNet technique) divides a WSI into several nonoverlapping patches of size 64 × 64 pixels. During training

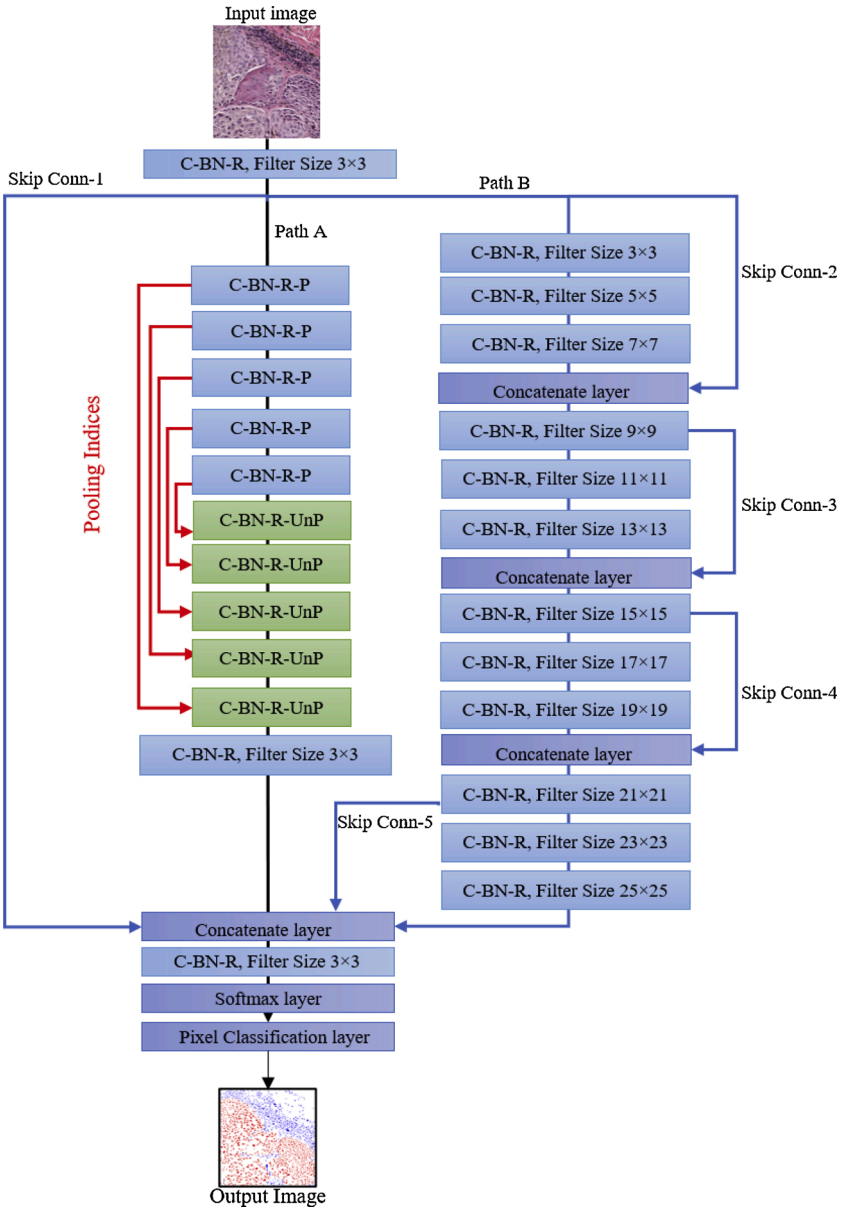

Fig. 3. The proposed INS-Net deep learning architecture. Note that in the output image the melanoma, non-melanoma nuclei, and background pixels are shown in red, blue and white colors, respectively.

these patches are labelled into 8 classes (e.g., stroma, complex stroma, normal). The ResNet-50 architecture is then trained to classify the patches. Although, the patch-based segmentation is fast (Sabol et al., 2021; Gadermayr et al., 2019), the technique might generate many false positive patches.

In this paper, we propose an automated technique to segment cutaneous malignant melanoma regions in H&E-stained images. In the proposed technique, the nuclei are first detected and segmented into melanoma and non-melanoma classes using a CNN architecture. The CMM regions are then generated by applying a series of morphological operations on the detected melanoma nuclei. The main difference between the existing methods and the proposed methods is that the existing methods work at patch level to detect the CMM regions whereas the proposed method first detects the nuclei and then builds up the CMM regions. The assumption here is that the melanoma nuclei can be detected with a higher accuracy, resulting in a superior overall segmentation performance.

The organization of the paper is as follows. Section 2 describes the dataset used to train and evaluate the proposed technique. Section 3 describes the proposed technique in detail. Section 4 presents the performance evaluation, followed by the conclusion in Section 5.

2. Data description

In this section, we present the details of the training and the testing dataset to evaluate the performance of the proposed nuclei segmentation

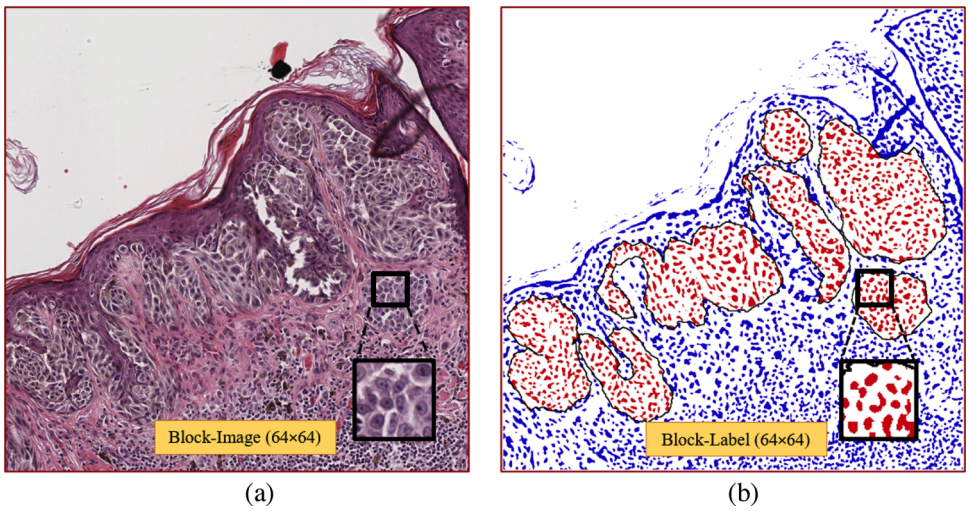

Fig. 4. Example of (a) an original H&E Image (960 × 960) and (b) the corresponding classified ground truth image, where the melanoma and non-melanoma nuclei appear in red and blue colors, respectively.

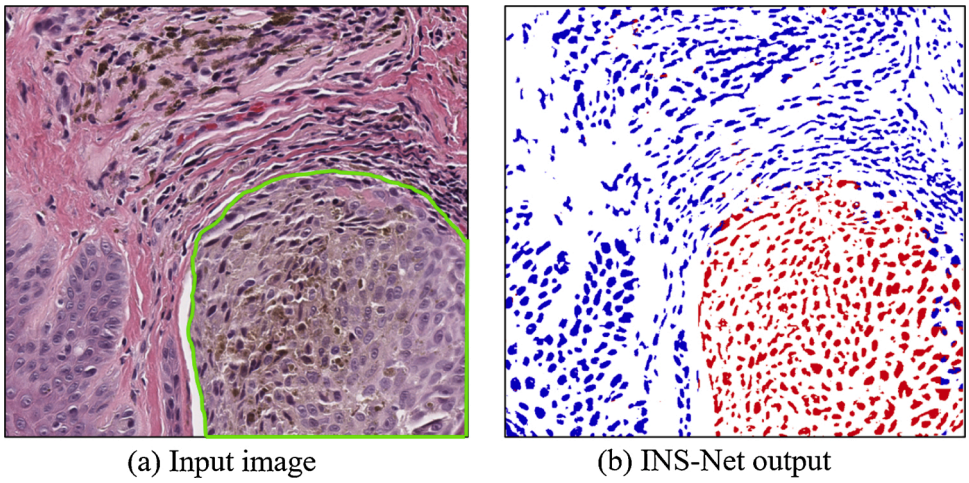

Fig. 5. Example of (a) an Original Image (in color) and (b) the corresponding INS-Net (segmented) output. The melanoma nuclei, non-melanoma nuclei, and the background pixels appear in red, blue and white colors, respectively.

and cell classification technique. The digitized biopsies were collected at the Cross Cancer Institute, University of Alberta, Edmonton, Canada in accordance with the protocol for the examination of the specimens with skin melanoma. Standard Neutral Buffered formalin-fixed paraffin-embedded tissue blocks of these biopsies were cut into thin slices (e.g., 4 μm for light microscope). These slices were then mounted to glass slides and stained using H&E stain (Haggerty et al., 2014). The WSIs were obtained by scanning the H&E slides using aperio scanscope scanning system under 40X magnification. The size of a WSI is typically around 40,000 × 60,000 pixels (0.25 μm/pixel resolution) and each WSI contains thousands of cell nuclei. The image dataset consists of 100 H&E-stained images with size (960 × 960 RGB pixels) extracted from 4 WSIs of skin tissue. The 100 H&E-stained images are divided into training (70), validation (15), and testing (15) datasets. Note that the ground truth melanoma regions of the H&E images were generated by matching MART-1 stained image of consecutive tissue sections (MART-1 is a sensitive and specific marker used for the diagnosis of melanoma). This limited the size of the dataset as only a handful of slides were available with both H&E and MART-1 stains.

3. Proposed technique

The schematic of the proposed technique is shown in Fig. 2 which consists of two modules: CNN-based nuclei segmentation and melanoma region detection. The details of these two modules are presented in the following.

3.1. CNN-based nuclei segmentation

In this module, the H&E-stained image is segmented into three regions: melanoma nuclei, non-melanoma nuclei and background regions. The segmentation is done by using the proposed CNN architecture

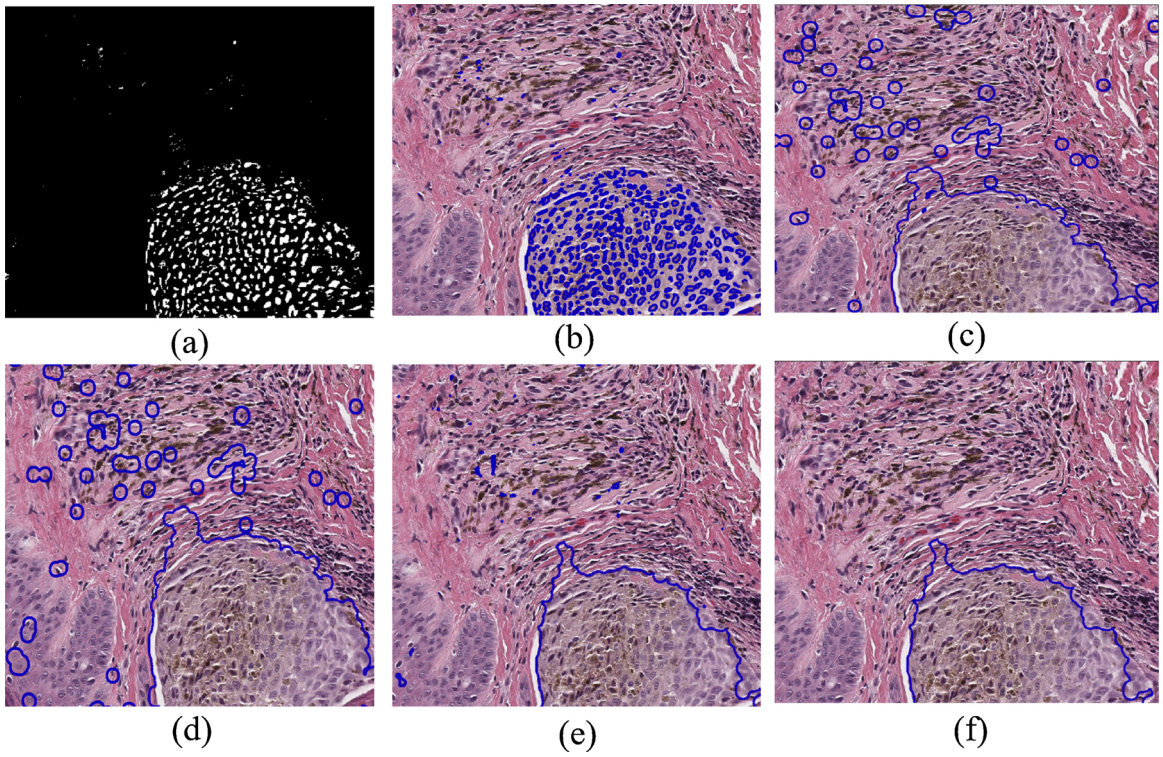

Fig. 6. Example of intermediate output images of the MRD module. Melanoma nuclei mask (a) obtained using the proposed CNN, (b) melanoma nuclei mask (in blue) superimposed on the original H&E image (c) after *dilation*, (d) after *image fill*, (e) after *erosion*, and (f) after *area thresholding* operations. In Figs. (b)–(f), the intermediate melanoma masks are superimposed on the H&E image to show more insights.

Table 2
Nuclei segmentation performance on H&E-stained images.

Techniques	Accuracy	Precision	Recall	Dice Coefficient
Voting + Watershed (Hongming et al., 2013)	83.64	78.24	84.64	81.31
gLoG + mRLS (Xu et al., 2017b)	76.67	79.27	60.25	68.46
SegNet (Badrinarayanan et al., 2015)	87.84	84.16	87.53	85.81
U-Net (Ronneberger et al., 2015)	78.79	87.41	57.87	69.63
NS-Net (Alheejawi et al., 2020)	90.21	87.20	89.90	88.52
INS-Net	94.12	90.32	88.05	89.17

Table 3
Configuration of the CNN architectures used in performance evaluation. Note that PBS-ResNet does patch-based segmentation directly and does not perform nuclei segmentation.

CNN Architecture	Convolutional layers	No. of Trained parameters	Filter size	No. of Filters per layer
SegNet (Badrinarayanan et al., 2015)	8	225,542	3 × 3	64
U-Net (Ronneberger et al., 2015)	11	905,472	3 × 3	(64, 128, 256)
NS-Net (Alheejawi et al., 2020)	5	150,336	(3 × 3)- (11 × 11)	64
PBS-ResNet (Sabol et al., 2021)	53	22,676,052	(1 × 1)- (7 × 7)	(64, 128, 256,512,1024, 2048)
INS-Net	18	225,987	(3 × 3)- (21 × 21)	64

shown in Fig. 3. The CNN architecture has 25 convolution layers instead of 5 layers in the NS-Net (Ronneberger et al., 2015) architecture used for nuclei segmentation. The proposed architecture, henceforth referred to as the improved NS-Net (INS-Net), consists of two paths: path A and path B. Out of 25 layers, 13 layers are in the path A, and 12 layers are in path B. Note that there are five Skip Connections (Skip Conn) in the proposed INS-Net to reduce the gradient vanishing impact (Kaiming et al., 2016).

There are 6 types of layers in INS-Net architecture and the details of these layers are explained in the following.

1 C-BN-R layer: This layer includes three operations: Convolution, Batch Normalization, and Rectified Linear Unit (ReLU) activation (Eigen and Fergus, 2015; Ioffe and Szegedy, 2015; Nair and Hinton, 2010).

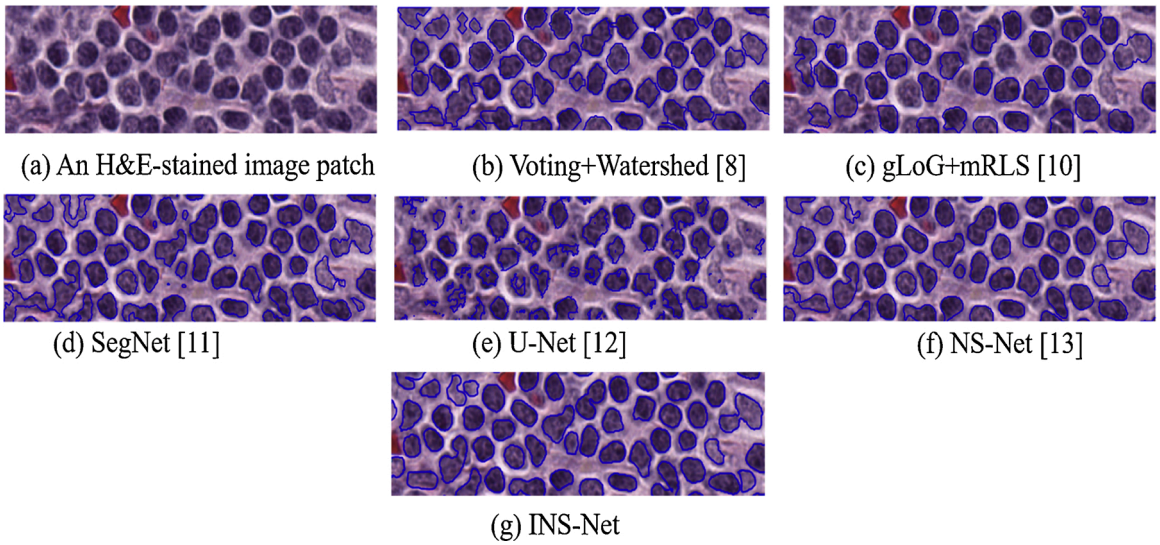

Fig. 7. Subjective comparison of cell nuclei segmentation results (contoured in blue color) (a) original test image, (b)-(g) Segmentation results for Voting + Watershed (Hongming et al., 2013), gLoG + mRLS (Xu et al., 2017b), SegNet (Badrinarayanan et al., 2015), U-Net (Ronneberger et al., 2015), NS-Net (Alheejawi et al., 2020) and the proposed INS-Net techniques, respectively.

2 C-BN-R-P layer: This layer consists of a C-BN-R layer followed by the Pooling operation to reduce the size (width x height) of the feature maps by selecting a pooling window and a stride value. In this work, we have used MAX pooling, window size of 2 × 2 and a stride of 2 × 2. Note that the index of the maximum value is sent to the corresponding C-BN-R-UnP layer.
3 C-BN-R-UnP layer: This layer consists of a C-BN-R layer followed by the UnPooling operation to upsample the feature map size (width x height). In this paper, an upsampling factor of 2 × 2 is used. The upsampling is done using the bilinear interpolation. The corresponding index from the C-BN-R-P layer is used to determine the location of the pixel that needs to be upsampled.
4 Concatenate layer: This layer combines the feature maps (of same size) from two or more input layers. The depth of the output layer is equal to the sum of depths of the input layers. In Fig. 3, this layer concatenates the output of paths A and B. In our implementation, outputs of paths A, B, and the Skip-Conn1 have depths of 64 each. In other words, the output of the Concatenate layer has a depth of 192.
5 SoftMax layer: This layer finds the probability values of each pixel for K classes. Note that each pixel will have K probability values (In this paper, $K = 3$) (Robert, 2014).
6 Pixel classification layer: This layer selects the class with the highest value of SoftMax output for each pixel.

In the INS-Net (see Fig. 3), it is observed that Path B is used to extract fine features of the cells and the background, whereas the Path A is used to extract coarse features of the cells and background regions. In this paper, the INS-Net architecture is used to segment the H&E-stained image pixels into melanoma nuclei, non-melanoma nuclei, and background pixels.

Note that the dataset contains 100 H&E-stained images each with size 960 × 960 as described in Section 2. Fig. 4(a) shows an example of a 960 × 960 image, and it can be observed that the image contains hundreds of nuclei. These 100 images are divided into training (70 images), testing (15 images) and validation (15 images) datasets. As it is computationally expensive to use the whole image as input to the CNN, each image is further divided into non-overlapping blocks of 64 × 64 color pixels to obtain 225 block-images (an example of a block-image is shown in Fig. 4). The total number of the obtained block-images is 22,500 (= 100 × 225). Out of these, 19,125 block-images are used for training and validation, and 3375 block-images are used for testing.

Fig. 5(a) shows an input H&E-stained image and the CMM region is shown with a green contour. The Nuclei Segmentation results obtained using the INS-Net architecture is shown in Fig. 5(b). It is observed that the nuclei in the CMM region (of Fig. 5(a)) have been detected accurately (the red nuclei) in Fig. 5(b). The accuracy of nuclei segmentation results is very important to determine the melanoma regions mask in H&E-stained images. The doctors can then determine the depth of the melanoma invasion and grade the melanoma based on the detected CMM regions. In the next section, the nuclei segmentation results will be used to generate the melanoma regions mask.

3.2. *Melanoma Region Detection (MRD)*

This module is used to determine the melanoma regions (MR) from the NS mask obtained using the INS-Net architecture. The MR detection consists of several morphological operations applied on the melanoma nuclei mask (see Fig. 6(a)). Note that the melanoma nuclei mask is a binary mask representing the melanoma nuclei class obtained from the NS mask (see the red pixels in Fig. 5(b)). The MR detection is done using the following steps.

1 The isolated melanoma nuclei (considered as foreground) in a neighbourhood are merged using the binary *morphological dilation* operation. In this work, a disc structuring element with 5–20 pixels radius is used. An example output is shown in Fig. 6(c). The merged regions will include the melanoma nuclei and its neighboring background pixels. Note that the size of structuring element gives a trade-off between precision and recall (or sensitivity). A larger structuring element is expected to provide higher sensitivity but lower precision.

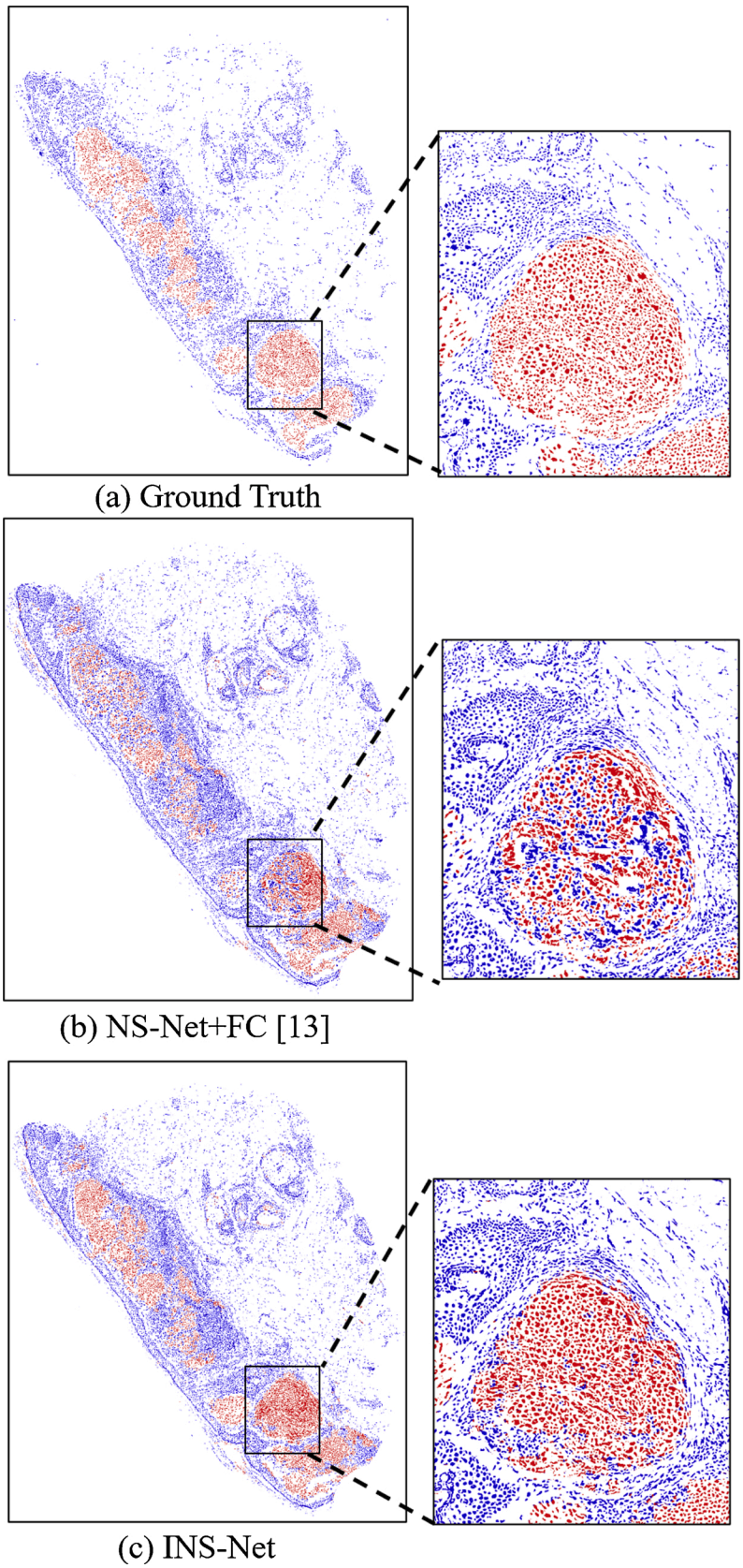

Fig. 8. Subjective comparison of nuclei classification results of the H&E-stained image shown in Fig. 1. (a) The ground truth image, nuclei, (b) NS-Net + FC classification result, and (c) the proposed INS-Net classification result.

Table 4
Nuclei classification performance.

Technique	Accuracy	Precision	Recall	Dice Coefficient	Jaccard score
NS-Net + FC (Alheejawi et al., 2020)	97.27	84.37	77.52	81.37	69.90
INS-Net (proposed)	99.33	85.79	87.31	86.48	76.54

2 Sometimes, there are small, isolated background pixels inside the merged melanoma regions, which can be considered as noise. An *image fill* operation is performed to change these isolated background pixels to the foreground pixels.
3 During the dilation operation (step 1), the size of an object typically increases. To nullify the increase in object size during dilation, an *erosion* operation is performed. The structuring element is same as that used in the step 1.
4 Connected melanoma regions with small areas are removed using an *area thresholding* method. In this paper, an area threshold of 600 pixels (equivalent to 150 μm^2 area) has been used to detect the noise regions.

Fig. 6 shows the examples of the intermediate results obtained by the above operations. It is observed that the output of the MRD module shows an excellent melanoma region segmentation compared with the ground truth image shown in Fig. 5(a). Note that we also implemented an MR generation technique by applying image closing followed by image fill and area threshold. But the overall performance is not as good as the MRD module.

4. Results and discussion

In this section, we present the performance of the proposed technique and compare it with state-of-the-art techniques. The performance of the Nuclei Segmentation module is presented first followed by the performance of MRM module.

4.1. Nuclei segmentation performance

In this section, the nuclei segmentation mask obtained by the INS-Net will be evaluated. The segmentation performance is evaluated using 3375 block-images (each with 64 × 64 pixels) as explained in Section 3.1. The segmentation performance of the INS-Net is evaluated for each pixel and compared with the handcrafted feature-based algorithms: gLoG + mRLS and Voting + Watershed techniques as well as CNN-based techniques using SegNet, U-Net and NS-Net architectures. The segmentation performance is evaluated using *Accuracy*, *Precision, Recall* (also known as *Sensitivity*), and *Dice Coefficient* (also known as *F1* score) measures defined as follows (Csurka et al., 2013):

$$Accuracy = \frac{TP + TN}{TP + FP + FN + TN} \times 100\%$$

$$Precision = \frac{TP}{TP + FP} \times 100\%$$

$$Recall = \frac{TP}{TP + FN} \times 100\%$$

$$Dice\ Coefficient = \frac{2 \times Precision \times Recall}{Precision + Recall} \times 100\%$$

where *TP*, *TN*, *FN* and *FP* denote the number of true positive, true negative, false negative and false positive pixels, respectively. Table 2 shows the segmentation performance of different techniques. It is observed that the deep learning algorithms provide an excellent performance compared to the conventional feature-based algorithms. This is because the conventional features are less sensitive to the diversity of the cell nuclei in the skin tissue. For example, the melanoma cells tend to have light and inhomogeneous color (see Fig. 1), which cause misdetection of the melanoma cells in the gLoG + mRLS and Voting + Watershed techniques.

In this work, the SegNet, U-Net and NS-Net and the proposed INS-Net architectures are trained with the same number of training images (70 H&E-stained images). The configuration of the CNN architectures is shown in Table 3. Fig. 7 shows the subjective segmentation performance of Voting + Watershed, gLoG + mRLS, SegNet, U-Net, NS-Net and the proposed INS-Net architecture. It is observed that the INS-Net architecture provides an excellent nuclei segmentation performance, whereas gLoG + mRLS, Voting + Watershed techniques miss a few cell nuclei due to the inhomogeneity in the cell nuclei color. It is also observed that the U-Net architecture does not perform well compared to the other techniques because of the overfitting of the large number of the filters that are used in the cell nuclei segmentation.

Fig. 8 shows visual examples of melanoma nuclei classification results using the NS-Net + FC, and the proposed INS-Net compared with the ground truth image. Note that in the NS-Net + FC technique an SVM classifier is used to detect the melanoma nuclei. The SVM uses a feature vector of length 54 (18 first-order features, 9 Histogram of Oriented Gradient features, 24 Haralick texture features and 3 Morphological features) calculated for each nucleus. For the proposed technique, the nuclei segmentation and classification are integrated in a single CNN architecture. In Fig. 8(c), it is observed that the INS-Net has superior nuclei classification results compared to the NS-Net + FC outputs shown in Fig. 8(b). The objective nuclei classification performance is shown in Table 4. It is observed that the proposed INS-Net provides a superior classification performance compared to the NS-Net + FC architecture. The mis-classification results of the melanoma nuclei can impact negatively on the subsequently obtained melanoma regions detected by the MRD module. Note that accurate melanoma nuclei classification results are important to obtain a good MR detection performance by the MRD module.

4.2. Melanoma Region Detection performance

In this section, the intermediate output images of the MRD module are evaluated after each operation. The melanoma segmentation performance of the proposed INS-Net + MRD is then compared with the output of PBS-ResNet (Sabol et al., 2021) and NS-Net + FC + MRD techniques. For the PBS-ResNet + MRD and INS-Net + MRD, a disc structuring element with 9 pixels radius is used whereas for the NS-Net + MRD technique, a disc structuring element with 16 pixels radius is used. The size of the structuring elements was selected so as to obtain the best performance.

The subjective performance of the MRD module in the NS-Net + FC + MRD technique and the proposed INS-Net + MRD technique are shown in Fig. 9. It is observed that the overall melanoma region detection performance of the proposed technique is superior to that obtained by the NS-Net + FC + MRD technique. This is primarily because the

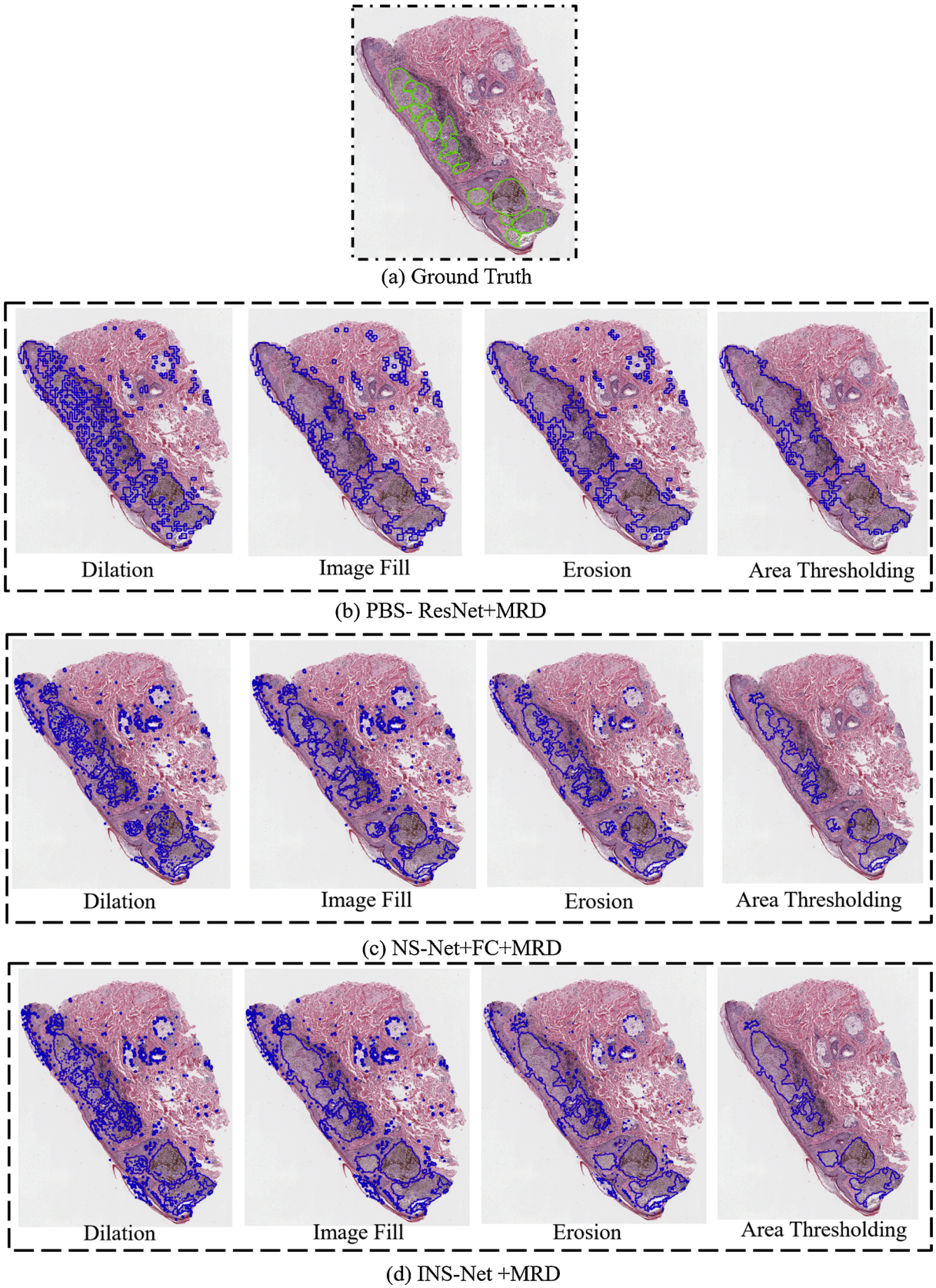

Fig. 9. Subjective comparison of MRD results (a) The ground truth image (b) Melanoma detection using the PBS-ResNet + MRD technique, (c) Melanoma detection using the NS-Net + FC + MRD technique and (d) Melanoma detection using INS-Net + MRD technique.

Table 5
Melanoma segmentation performance of various steps of the MRD module.

Steps	Accuracy	Precision	Recall	Dice Coefficient
Dilation	95.14	80.27	49.87	61.55
Dilation + Image Fill	94.66	69.88	88.25	78.00
Dilation + ImageFill + Erosion	95.80	76.35	85.97	80.88
Dilation + ImageFill + Erosion + AreaThresh	97.70	83.22	87.08	85.10

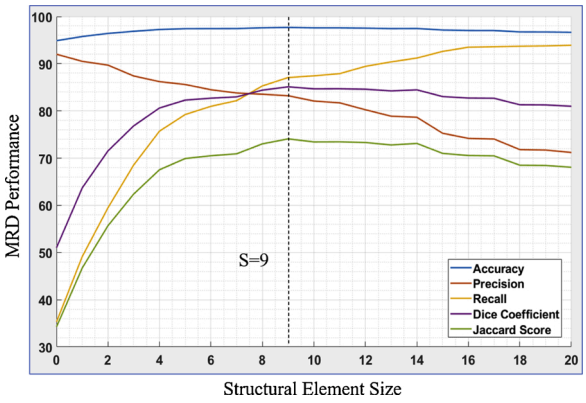

Fig. 10. MRD performance with different structural element.

accuracy of the melanoma nuclei classification of the NS-Net + FC technique is not very high.

The MRD module is now objectively evaluated in terms of Accuracy, Precision, Recall, and Dice coefficient. Table 5 shows the ablation study of the different steps for the melanoma segmentation performance of the MRD module. It is observed that the performance improves with each added step. The overall performance of the MRD module (with all four steps) is shown in the last row of the table. It is observed that a Dice coefficient of 83.81 % is achieved by the MRD module.

The melanoma regions detected by the proposed INS-Net + MRD technique are now compared with those obtained by the state-of-the-art techniques: PBS-ResNet (Sabol et al., 2021) and NS-Net + FC + MRD. In the PBS-ResNet, the H&E WSI is first divided into non-overlapping blocks of size 64 × 64 (RGB) pixels. Note that other block sizes (e.g., 32 × 32, 48 × 48, 80 × 80 128 × 128) have also been experimented with and 64 × 64 block size provide the best performance. Each block is then classified into melanoma, non-melanoma, and background blocks using the ResNet-50 CNN classifier. The ResNet-50 CNN classifier has been trained with 19,016 images for each of the three classes. In the NS-Net + FC + MRD technique, the melanoma nuclei in an H&E WSI are detected using the NS-Net + FC technique (Alheejawi et al., 2020), which uses the NS-Net for the nuclei segmentation followed by nuclei classification (to detect the melanoma nuclei) using SVM. The detected melanoma nuclei are then passed through the MRD module to obtain the melanoma regions.

In this paper, we also evaluate the performance of the MRD module with different size (S) of the structuring element. Fig. 10 shows the performance of MRD module in INS-Net + MRD technique. It is observed that the performance of INS-Net + MRD technique is very sensitive to the value of S. This is expected as melanoma regions are dilated and connect, the Recall values increase. Note that the best performance in terms of Accuracy, Precision, Recall, Dice Coefficient and Jaccard Score is obtained with S = 9. In this paper, the MRD module is also used in the PBS-ResNet + MRD and Net + FC + MRD techniques. It has been found that the best performance for PBS-ResNet + MRD and Net + FC + MRD techniques is obtained with disc structuring elements of radius of 9 and 16 pixels, respectively.

Fig. 11 shows a visual example of the melanoma region detection on the H&E WSI shown in Fig. 1. It is observed that the PBS-ResNet generates a significant number of FP and FN regions throughout the image due to the misclassification of patches (of size 64 × 64). The NS-Net + FC + MRD generates a significant number of FP and FN pixels due to the misclassification of melanoma nuclei. On the other hand, the INS-Net + MRD provides a superior segmentation performance. This is because the technique first classifies the melanoma nuclei and builds the melanoma region by merging the detected nuclei resulting in a superior performance.

The segmentation performance is now compared objectively with respect to Accuracy, Precision, Recall, Dice Coefficient (defined before) as well as Jaccard score as defined below.

$$Jaccard\ Score = \frac{TP}{TP + FP + FN} \times 100\%$$

Table 6 shows the melanoma segmentation performance of the proposed technique and state-of-the-art techniques. It is observed that the proposed INS-Net + MRD has superior results in terms of Precision, and Accuracy compared to that of the PBS-ResNet and NS-Net + FC + MRD techniques. The INS-Net + MRD shows the best performance over the PBS-ResNet and NS-Net + FC + MRD techniques.

The run-time complexity of the various melanoma region detection techniques is shown in the last column of Table 6. The average execution time (for both nuclei segmentation and melanoma detection) for a WSI in testing mode is calculated. In this paper, all techniques were implemented using MATLAB R2020a and run on a Windows 10 workstation with Intel i7−6700 K CPU, 12 GB RAM, and NVIDIA GeForce GTX 745 graphic card. Note that the CNNs were implemented using the Deep Network Designer Toolbox.

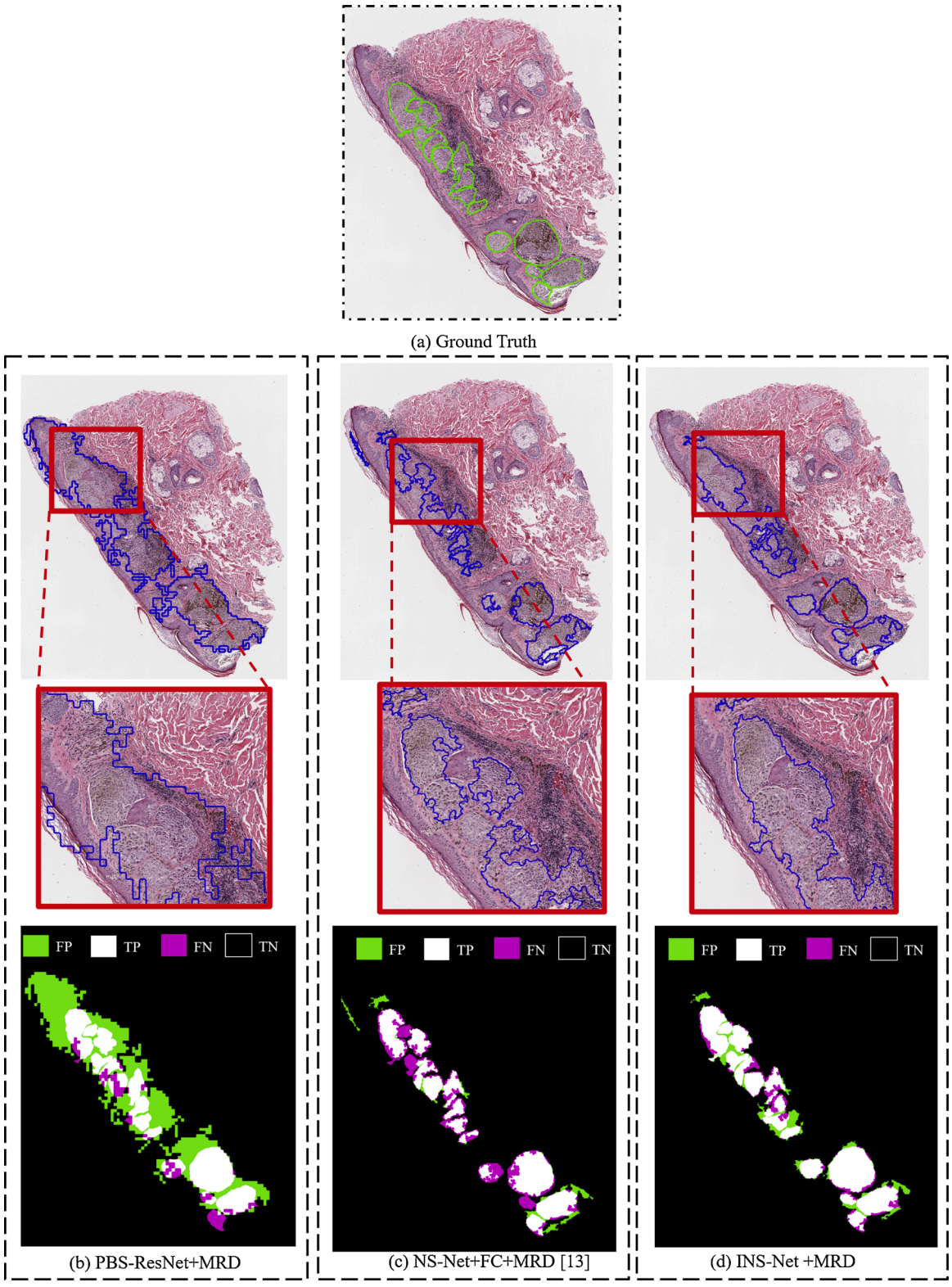

Fig. 11. Subjective comparison of the detected melanoma regions. (a) The ground truth segmentation mask (green contour), melanoma regions detected by (b) PBS-ResNet + MRD, (c) NS-Net + FC + MRD, and (d) INS-Net + MRD. The melanoma regions are shown with blue contour. The last row shows the FP (green), TP (green), FN (red) and TN (black) regions. In the upper row in Fig. (b), the melanoma regions are shown with light blue shade.

The PBS-ResNet (Sabol et al., 2021) requires the lowest execution time (about 184 s) as it classifies the patches directly. On the other hand, the NS-Net + FC + MRD (Alheejawi et al., 2020) requires the highest execution time (about 1034 s). Note that in this technique the FC (for Feature extraction and Classification) takes about 50 % of the overall execution time. The CNN segmentation architecture requires more time compared to the CNN classifiers as the CNN segmentation classifies each pixel in the image instead of classifying the whole patch. The proposed INS-Net + MRD technique also requires a long execution time (about 402 s) due to the nuclei-based segmentation. However, an increase in

Table 6
Melanoma region detection performance.

Technique	Accuracy	Precision	Recall	Dice Coefficient	Jaccard score	Execution time (in s)
PBS-ResNet + MRD (Sabol et al., 2021)	89.78	68.14	83.88	75.19	66.26	**184**
NS-Net + FC + MRD[a] (Alheejawi et al., 2020)	95.521	80.11	84.36	81.95	70.21	1034
INS-Net + MRD (proposed)	**97.70**	**83.22**	**87.08**	**85.10**	**74.07**	402

[a] The MRD module has been added to (Alheejawi et al., 2020) for generating the melanoma regions.

the computational complexity is offset by the superior melanoma region detection performance of the proposed technique.

The performance of the melanoma region detection as shown in Table 6 shows a significant improvement over the state-of-the-art techniques. However, it is acknowledged that the training and testing dataset used in this work is small as explained in Section 2. More experiments are planned in future with larger dataset of images to demonstrate the generalizability of the proposed technique.

5. Conclusions

This paper proposes an automated technique to detect cutaneous malignant melanoma regions in skin tissue images stained with H&E. The technique segments the cell nuclei in H&E-stained images using the proposed INS-Net deep learning network. The INS-Net segments the image into melanoma nuclei, non-melanoma nuclei and background regions. The segmented melanoma nuclei are then used to generate a melanoma mask using the melanoma region detection (MRD) module. Experimental results with a small melanoma dataset show that the proposed method can achieve a nuclei segmentation accuracy of over 94 %. The malignant melanoma regions are detected with a Dice coefficient of around 85 % (precision of 83 % and recall of 87 %), which is substantially better than the state-of-the-art techniques. The proposed technique also has a small execution time, about 6−7 min for an image with a standard desktop computer, making it suitable for clinical diagnosis with a fast turnaround time.

Author statement

The contributions of the authors are given below.

Salah Alheejawi: Conceptualization, Methodology, Software, Formal analysis, Investigation, and Writing-original draft preparation.

Richard Berendt: Conceptualization, Resources, and Data Curation.

Naresh Jha: Conceptualization, Resources, and Data Curation.

Santi P. Maity: Software, Analysis, and Writing - review & editing.

Mrinal Mandal: Conceptualization, Supervision, Writing - review & editing, Project administration, and Funding acquisition.

Acknowledgment

We acknowledge the support of the Natural Sciences and Engineering Research Council of Canada (NSERC) (Grant number RGPIN-2020-05873). We also acknowledge scholarship support from the Ministry of Higher Education and Scientific Research (MOHESR), Iraq and Imam Ja'afar Al Sadiq University, Iraq.

References

Alheejawi, Salah, Berendt, Richard, Jha, Naresh, Mandal, Mrinal, 2019. Novel lymph node segmentation and proliferation index measurement for skin melanoma biopsy images. Comput. Med. Imaging Graph. 73, 19–29.

Alheejawi, Salah, Berendt, Richard, Jha, Naresh, Mandal, Mrinal, 2020. Melanoma Cell Detection in Lymph Nodes Histopathological Images using Deep Learning. 2020). Signal & Image Process.: An Int. J. (SIPIJ) 11 (4, August).

Badrinarayanan, Vijay, Kendall, Alex, Cipolla, Roberto, 2015. SegNet: A Deep Convolutional Encoder-Decoder Architecture for Image Segmentation. arXiv. Preprint arXiv: 1511.0051.

Brochez, Lieve, Verhaeghe, Evelien, Grosshans, Edouard, et al., 2002. Inter-observer variation in the histopathological diagnosis of clinically suspicious pigmented skin lesions. J. Pathol. 196 (4), 459–466.

Cheng, Lu, Mandal, Mrinal, 2015. Automated analysis and diagnosis of skin melanoma on whole slide histopathological images. Pattern Recogn. 48 (August 2015), 2738–82750, 8.

Cheng, Lu, Mahmood, Muhammad, Jha, Naresh, Mandal, Mrinal, 2012. A robust automatic nuclei segmentation technique for quantitative histopathological image analysis. Anal. Quant. Cytopathol. 34 (6 December), 296–308.

Csurka, Gabriela, Larlus, Diane, Perronnin, Florent, 2013. What is a good evaluation measure for semantic segmentation? Proc. of the British Machine Vision Conference 32.1–32.11.

Eigen, David, Fergus, Rob, 2015. Predicting depth, surface normals and semantic labels with a common multi-scale convolutional architecture. Proceedings of the International Conference on Computer Vision 2650–2658.

Gadermayr, Michael, Dombrowski, Ann-Kathrin, Klinkhammer, Barbara Mara, Boor, Peter, Merhof, Dorit, 2019. CNN cascades for segmenting sparse objects in gigapixel whole slide images. Comput. Med. Imaging Graph. 71, 40–48.

Haggerty, Juliana M., Wang, Xiao N., Dickinson, Anne, O'Malley, Chris J., Martin, Elaine B., 2014. Segmentation of epidermal tissue with histopathological damage in images of haematoxylin and eosin-stained human skin. BMC Med. Imaging 14 (1), 7.

Hongming, Xu, Cheng, Lu, Mandal, Mrinal, 2013. An efficient technique for nuclei segmentation based on ellipse descriptor analysis and improved seed detection algorithm. IEEE J. Biomed. Health Inf. 18 (5), 1729–1741.

Ioffe, Sergey, Szegedy, Christian, 2015. Batch normalization: accelerating deep network training by reducing internal covariate shift. Proceedings of the 32nd International Conference on Machine Learning 37, 448–456, 2015.

Kaiming, He, Xiangyu, Zhang, Shaoqing, Ren, Jian, Sun, 2016. Deep residual learning for image recognition. IEEE Conference on Computer Vision and Pattern Recognition (CVPR), Las Vegas, NV, USA 770–778.

Lu, Cheng, Mahmood, Muhammad, Jha, Naresh, Mandal, Mrinal, 2013a. Automated segmentation of the melanocytes in skin histopathological images. IEEE J. Biomed. Health Inf. 17 (2), 284–296.

Lu, Cheng, Mahmood, Muhammad, Jha, Naresh, Mandal, Mrinal, 2013b. Detection of melanocytes in skin histopathological images using radial line scanning. Pattern Recognit. 46 (2, February), 509–518.

Nair, Vinod, Hinton, Geoffrey E., 2010. Rectified linear units improve restricted boltzmann machines. Proceedings of the 27th International Conference on Machine Learning 807–814.

Robert, Christian, 2014. Machine learning, a probabilistic perspective. CHANCE 27 (2), 62–63.

Rojo, Marcial G., Castro, Ana M., Gonçalves, Luis, 2011. COST action "eurotelepath": digital pathology integration in electronic health record, including primary care centres. Diagn. Pathol. 6 (S6), S1–6 (2011).

Ronneberger, Olaf, Fischer, Philipp, Brox, Thomas, 2015. U-net: convolutional networks for biomedical image segmentation. Med. Image Comput. Comput. Assist. Interv. 9351, 234–241.

Patrik Sabol, Peter Sinčák, Pitoyo Hartono, Pavel Kočan, Zuzana Benetinová, Alžbeta Blichárová, Ľudmila Verbóová, Erika Štammová, Antónia Sabolová-Fabianová, and Anna Jašková, "Explainable classifier for improving the accountability in decision-making for colorectal cancer diagnosis from histopathological images" Journal of Biomedical Informatics, Vol. 109.

Weinstein, Ronald S., Graham, Anna R., Richter, Lynne C., et al., 2009. Overview of telepathology, virtual microscopy, and whole slide imaging: prospects for the future. Hum. Pathol. 40 (8), 1057–1069.

Xu, Hongming, Lu, Cheng, Berendt, Richard, Jha, Naresh, Mandal, Mrinal, 2017a. Automatic nuclei detection based on generalized Laplacian of Gaussian filters. IEEE J. Biomed. Health Inf. (JBHI) 21 (3), 826–837.

Xu, Hongming, Lu, Cheng, Berendt, Richard, Jha, Naresh, Mandal, Mrinal, 2017b. Automatic nuclear segmentation using multi-scale radial line scanning with dynamic programming. Accepted for publication by IEEE Trans. Biomed. Eng. 64 (10 October), 2475–2485.